Acta Materialia 178 (2019) 163–172

Contents lists available at ScienceDirect

Acta Materialia

journal homepage: www.elsevier.com/locate/actamat

Full length article

Thermodynamic assessment of the solar-to-fuel performance of $La_{0.6}Sr_{0.4}Mn_{1-y}Cr_yO_{3-\delta}$ perovskite solid solution series

Alexander H. Bork [a, b], Erwin Povoden-Karadeniz [d], Alfonso J. Carrillo [a, b], Jennifer L.M. Rupp [a, b, c, *]

[a] Electrochemical Materials, Department of Materials Science, ETH Zurich, Hönggerbergring 64, 8093, Zürich, Switzerland
[b] Electrochemical Materials Laboratory, Department of Materials Science and Engineering, Massachusetts Institute of Technology, Cambridge, MA, USA
[c] Electrochemical Materials Laboratory, Department of Electrical Engineering and Computer Science, Massachusetts Institute of Technology, Cambridge, MA, USA
[d] Christian-Doppler Laboratory Interfaces and Precipitation Engineering CDL-IPE, Institute of Materials Science and Technology, TU Wien, Vienna, Austria

ARTICLE INFO

Article history:
Received 22 November 2018
Received in revised form
7 July 2019
Accepted 15 July 2019
Available online 18 July 2019

Keywords:
Solar-to-fuel
Thermochemical cycling
Chromium doped lanthanum strontium manganite
Perovskite
Defect modeling

ABSTRACT

In the search of new materials for the solar-to-fuel technology, we turn to the material class of perovskites that offer wide possibilities in manipulation of its chemistry and redox activity. Here, we access the role of Cr in the $La_{0.6}Sr_{0.4}Mn_{1-y}Cr_yO_{3-\delta}$ perovskite solid solution hitherto unexplored for two-step solar thermochemical fuel production. A multi-component Calphad defect model for the system La–Sr–Cr–Mn–O is therefore optimized and used for computations of oxygen nonstoichiometries and redox thermodynamics of the $La_{0.6}Sr_{0.4}Mn_{1-y}Cr_yO_{3-\delta}$ solution series in the temperature range of 1073–1873 K as a potential operation window for solar-to-fuel conversion. Modeling results reveal two advantages of substituting manganese by chromium. Firstly, it is possible to reduce the heat capacity with up to 10%, to a value of 132 J mol^{-1} K^{-1}. Secondly, the thermodynamic driving force for solar-to-fuel conversion increases and the Cr-doped materials provide higher yield and efficiency at isothermal operation. The proposed model allows for continuous simulative scanning of redox thermodynamics from zero Cr-doping to a fully substituted chromite perovskite. For isothermal water splitting, the composition $La_{0.6}Sr_{0.4}Mn_{0.2}Cr_{0.8}O_{3-\delta}$ displays the highest fuel yield and efficiency of 2.7% due to a high thermodynamic driving force at elevated temperature for this composition. These predictive insights give prospects for engineering the thermodynamics of the oxygen release reaction in perovskites towards higher fuel production and efficiency in solar-to-fuel reactors with isothermal operation.

1. Introduction

Solar-driven thermochemical dissociation of CO_2 and H_2O to syngas presents an attractive avenue away from dependence on fossil fuels [1,2]. Intermittent solar energy may be stored in chemical fuels and distributed on demand for transportation whilst mitigating CO_2 emissions. The working principle of two-step solar thermochemical fuel production may be exemplified by the changes in the oxygen nonstoichiometry, δ, of a perovskite with the general structure $ABO_{3-\delta}$. In the first step, at a temperature of 1623 K the perovskite oxide is reduced by solar thermal energy and typically with an inert sweeping gas to lower the oxygen partial pressure [3–6] and oxygen is released

$$ABO_3 \leftrightarrow ABO_{3-\delta} + \frac{\delta}{2}O_2(g) \quad (1)$$

Through a second step, the perovskite is oxidized in the presence of H_2O and CO_2, thus producing hydrogen and carbon monoxide (syngas) at a temperature of 1273 K through the following reactions:

$$ABO_{3-\delta} + \delta H_2O(g) \leftrightarrow ABO_{3-\delta} + \delta H_2(g) \quad (2a)$$

$$ABO_{3-\delta} + \delta CO_2(g) \leftrightarrow ABO_{3-\delta} + \delta CO(g) \quad (2b)$$

The produced syngas (H_2 + CO) in a solar thermochemical reactor may be converted into hydrocarbon fuels by commercial

* Corresponding author. Electrochemical Materials, Department of Materials Science, ETH Zurich, Hönggerbergring 64, 8093, Zürich, Switzerland.
E-mail address: jrupp@mit.edu (J.L.M. Rupp).

https://doi.org/10.1016/j.actamat.2019.07.022
1359-6454/

Fischer-Tropsch process [7]. A recent simulation of 1 MW_{th} thermochemical syngas production plant, working under realistic solar conditions for different locations in Australia, showed a maximum efficiency of 9.68% using state-of-the-art nonstoichiometric CeO_2 [8]. Nowadays researchers aim at finding new efficient and stable materials to perform thermochemical water and carbon dioxide splitting. Perovskites have received significant attention due to a high fuel production [3,4,9–15]. McDaniel et al. [3] revealed that (La,Sr)MnO_3 perovskites doped with Al on the B-site produced 9 times more H_2 and 6 times more CO compared to state-of-the-art material, ceria, when reduced at 1623 K and oxidized at 1273 K. Although these results are promising, it is worth noting that a large excess of steam and carbon dioxide is in general necessary to obtain high a CO and H_2 production for perovskites [16]. Thermodynamic analysis based on thermogravimetric experiments have shown that the to date studied perovskites $ABO_{3-\delta}$ (A = La, Sr, Ca, and B = Mn, Al) have a lower mass specific fuel productivity and efficiency compared to ceria under most operating conditions including two-step cycling and isothermal operation [6,16–20]. The lower efficiency of the perovskites is due to a high heat capacity and in particular a low absolute value of the Gibbs energy change of oxygen vacancy formation, which favours the reduction reaction but is unfavourable for the oxidation reaction.

This work employs thermodynamic computation to make a predictive investigation of the multicomponent perovskite $La_{0.6}Sr_{0.4}Mn_{1-y}Cr_yO_3$ as a new candidate for the solar-to-fuel application. Chromium is added to the B-site of the ABO_3 perovskite with the incentive to increase Gibbs energy change of oxygen formation and lower the heat capacity and to test whether those changes enhance the perovskite's efficiency compared to $La_{0.6}Sr_{0.4}MnO_3$

We fix the strontium content of 0.4 on the A-site [4,21] and systematically alter the ratio between chromium and manganese on the B-site. The strontium content of 0.4 is chosen to introduce a high concentration of acceptor type doping [22] inducing a high oxygen nonstoichiometry, while staying within the limits of Sr doping for a single-phase perovskite [21]. As shown by Devi et al. [21], a higher Sr content than 0.5 in $La_{1-x}Sr_xCrO_3$, may result in the formation of two phases $LaCrO_3$ and $SrCrO_4$. Recently, we presented and verified a new approach using computational thermodynamics with an optimized Calphad defect model of the perovskite $La_{1-x}Sr_xMnO_3$ [20,23]. Here, we propose an optimal composition of an extended perovskite with two A-site (La,Sr) and two B-site (Mn,Cr) dopants for improved efficiency of two-step solar thermochemical fuel production by thermodynamic and defect chemistry computation. The evaluation will be used to examine the trade-off between oxygen release, heat capacity, and favorability for water splitting to hydrogen and analyze the implications on the efficiency. The analysis is carried out for conventional two-step cycling with reduction at 1773 K and oxidation temperature at 1073 K. Besides temperature swing cycles, two-step solar thermochemical redox cycles can also be operated isothermally. In a recent review, Al-Shankiti et al. [24] evaluated different solar thermochemical reactor concepts. They concluded that pure isothermal thermochemical cycling is simpler, but less efficient theoretically. The advantage is that isothermal operation may simplify the reactor design, with less stress on the active and containing materials and alleviate the need for solid-solid heat recuperation [14,24]. The disadvantage of isothermal cycling is that a higher concentration of oxidizer is necessary because of a reduced thermodynamic driving force at high temperature for both ceria and the tested perovskites. To realize isothermal thermochemical cycling thus calls for materials that have a higher thermodynamic driving for oxidation at elevated temperature. We therefore also test the perovskites isothermally to test the material's performance under such conditions.

2. Modeling approach

For the modeling approach utilized in this work, it is important to distinguish between the *thermodynamics of the perovskite phase* formation, being represented by its Gibbs energy, and the *thermodynamics of the oxygen release reaction*. In essence, the Calphad approach is used to determine the equilibrium thermodynamics of the perovskite phase, which relies on an optimization towards the available experimental data. Since reduced compounds are also defined in the Calphad model of the perovskite phase, defect chemistry can also be simulated, aside of its molar enthalpy, entropy and heat capacity.

From the Calphad model of oxygen nonstoichiometry, we are able to derive the thermodynamics of the oxygen release reaction, which contains the Gibbs free energy, enthalpy and entropy of the oxygen release reaction. Using those parameters it is possible make a successful thermodynamic assessment including the materials' fuel production and efficiency [20].

2.1. Defect chemistry model of $La_{1-x}Sr_xMn_{1-y}Cr_yO_{3-\delta}$

In the Calphad model of $La_{1-x}Sr_xMn_{1-y}Cr_yO_{3-\delta}$ perovskite [25], which is represented by the formula $[La^{3+}, Sr^{2+}]^A[Mn^{2+}, Mn^{3+}, Mn^{4+}, Cr^{3+}, Cr^{4+}]^B[O^{2-}, Va^0]_3$, the solution of Sr^{2+} on La^{3+} sites in $La_{1-x}Sr_xMn_{1-y}Cr_yO_{3-\delta}$ results in charge deficiency, which (in air) is mainly compensated by oxidation of either Mn^{3+}/Mn^{4+} or Cr^{3+}/Cr^{4+}. In Kröger-Vink notation this can be expressed for changes in Mn as

$$La_{La}^{\times}Mn_{Mn}^{\times}O_3 \xrightarrow{Sr(La)} Sr'_{La}Mn_{Mn}^{\bullet}O_3 \tag{3}$$

Here, $La_{La}^{\times}$ signifies a lanthanum ion on lanthanum site with neutral charge, while Sr'_{La} indicates a strontium ion on a lanthanum site with a single negative charge, and $Mn_{Mn}^{\bullet}$ is a manganese ion at the B-site ABO_3 perovskite lattice with a single positive charge. The mechanism for reduction is change of the oxidation state of the B-site cation, followed by formation of oxygen vacancy ($V_O^{\bullet\bullet}$) defect according to.

$$O_O^x + 2Mn_{Mn}^{\bullet} \leftrightarrow V_O^{\bullet\bullet} + 2Mn_{Mn}^{\times} + 1/2O_2(g) \tag{4a}$$

$$O_O^x + 2Cr_{Mn}^{\bullet} \leftrightarrow V_O^{\bullet\bullet} + 2Cr_{Mn}^{\times} + 1/2O_2(g) \tag{4b}$$

In fact, it has been shown experimentally that manganese on the perovskite B-site is more prone to oxidation state changes compared to chromium for lower Sr contents of $x < 0.3$ in $La_{1-x}Sr_xMn_{0.5}Cr_{0.5}O_{3-\delta}$ [26,27]. However, defect evolution of the end-member $La_{1-x}Sr_xCrO_{3-\delta}$ compound of the perovskite solid solution also involves Cr^{4+}, aside of oxygen vacancies [28]. Moreover, we consider high strontium contents of $x = 0.4$ on the A-site and high chromium concentrations of up to $y = 0.9$, so also chromium will change oxidation state to maintain charge neutrality. Therefore, we include Cr^{4+} in the model as well.

2.2. Thermodynamic modeling of perovskite solution phase using reciprocal compound energy relations

The thermodynamics of a multi-component perovskite oxide solid solution is comprised of the stoichiometrically weighted sum of Gibbs energy functions of ternary perovskite compounds ABO_3. Its general form being presented in Eq. (5)

$$^{\circ}G_m^{prv} = \sum_i \sum_j \sum_k y_i y_j y_k {}^{\circ}G_{i:j:k} + \frac{1}{\sum_s n^{(s)}} RT \sum_s \sum_i n^{(s)} y_i^{(s)} \ln y_i^{(s)} + {}^{E}G_m^{prv} \quad (5a)$$

where the last term ${}^{E}G_m^{prv}$ describes the excess, non-ideal Gibbs interaction energy of mixing of different species on one sublattice

$${}^{E}G_m^{prv} = \sum_s \sum_i \sum_j y_i^{(s)} y_j^{(s)} \sum_{r \neq s} \sum_k y_k^{(r)} L_{i,j:\ldots:k} \quad (5b)$$

In Eq. (5a) the variable y_i is the site fraction of each cation on the A-sublattice, y_j is the site fraction of each cation on the B-sublattice, and y_k is the site fraction of O^{2-} and Va on the anion sublattice. $R = 8.31451\ J\ mol^{-1}\ K^{-1}$, $n^{(s)}$ are stoichiometric coefficients relating the sublattices. The second-last term accounts for the configurational entropy of mixing. In the present perovskite description, simultaneous interactions of ions on A- and B-sublattices of the perovskite phase are represented by the term in Eq. (5b). The parameters of the compound energy formalism are the stoichiometrically weighted Gibbs energies of the end-member compounds $^{\circ}G_{i:j:k}$.

In terms of optimizable parameter description, $^{\circ}G_{i:j:k}$ can be represented by a Gibbs energy polynomial. An ABO_3 perovskite line compound phase is simply written as

$$G_m^{ABO3} = a + bT + cT \ln T + dT^2 + eT^3 + fT^{-1} \quad (6)$$

and, since

$$\Delta H = \Delta G + TS = a - cT - dT^2 - 2eT^3 + 2fT^{-1} \quad (7)$$

one obtains an equation for the heat capacity

$$C_p^{prv} = (\partial H/\partial T) = T(\partial S/\partial T) = -c - 2dT - 6eT^2 - 2fT^{-2} \quad (8)$$

Model parameters *c, d, e, f* in Eq. (8) are adjusted by experimental heat capacities, whereas *a* and *b* (Eq. (6)) are related to enthalpy and entropy, respectively. Heat capacities of multi-component perovskite are, as a reasonable approximation of negligible "non-ideal" heat capacity contributions, simply defined by Neumann Kopp's rule [27], i.e. stoichiometrically and charge-balanced weighted sum of compound heat capacities.

Describing a continuous Gibbs energy of a perovskite solid solution from oxidized to reduced conditions requires stoichiometrically proper summing up of end-member compounds, obeying charge neutrality. In fact, the present multi-component perovskite sublattice formula $[La^{3+}, Sr^{2+}]^A[Mn^{2+},Mn^{3+},Mn^{4+},Cr^{3+},Cr^{4+}]^B[O^{2-}, Va^0]_3$ delivers (by simple recombination: ABO_3, $ABVa_3$ compounds) 20 end-member compounds, with only two of them showing charge-neutrality, as illustrated by the simple geometric representation of the perovskite phase, Fig. 1. Neutral compounds of the La–Sr–Cr–Mn oxide perovskite solid solution span the charge neutrality plane, which represents potentially realized mixed-valence perovskite in the scope of changing redox conditions. Two corner compositions of the neutral plane, $S2O_{2/3}Va_{1/3}$ and $L2O_{5/6}Va_{1/6}$ are defined by combinations of charged perovskite end-member compounds, e.g. S2O represents $Sr^{2+}Mn^{2+}(O^{2-})_3$. Realization of physically meaningful parametrization of 20 compound energies, most of them being charged, is indeed arguable. An appropriate diminution of parameters is obtained by the following considerations on reciprocal relations among end-member compounds.

For a general 4-component solution phase (A,B)(C,D), the reciprocal system of compound A:B, A:D, B:C, B:D Gibbs energies can be set up as these end-members representing the corners of a simple "composition square". According to Hillert [29], a solution phase with composition $(A_{0.25}B_{0.25})(C_{0.25}D_{0.25})$, i.e. lying in the center of the square will tend to decompose to either (A:C) and (B:D) compounds or (A:D) and (B:C) compounds. The driving force of this de-mixing is defined by the reciprocal reaction parameter,

$$^{\circ}G_r = {}^{\circ}G(A:D) + {}^{\circ}G(B:C) - {}^{\circ}G(A:C) - {}^{\circ}G(B:D). \quad (9)$$

The present case multi-component perovskite consists of a number of reciprocal systems, such as L4O-L4V–S4O–S4V in Fig. 1 Reciprocal systems of the perovskite phase, as represented by each of the square faces of the composition body, Fig. 1, comprise mostly charged and thus purely virtual corner compounds. Since the charged compounds are unlikely to form it is a reasonable and a successful modeling strategy to set $^{\circ}G_r$ equal to zero [21]. Setting the sum of this term to zero sets a useful constraint on the interaction energy parameters.

By the reciprocal relations approach, the thermodynamics of the whole perovskite solid solution is defined, still accepting ideal mixing among species in one sublattice. Whether this assumption is legitimate, is directly revealed by comparison of experimental defect chemistry data with the modeling results. In the present case of $La_{1-x}Sr_xMn_{1-y}Cr_yO_{3-\delta}$ perovskite, interactions representing non-ideal mixing among Cr^{3+} and Mn^{3+} or Mn^{4+} are introduced in the model, since an offset between experimental oxygen non-stoichiometries and modeling results was found by ideal model extension from quaternary subsystems to quinternary La–Sr–Cr–Mn–O. For the fitting procedure of these interaction energies, $L_{i,j:\ldots:k}$ in Eq. (5), we use Redlich-Kister [30] polynomials.

$$L_{La+3,Sr+2:Cr+3,Mn+3:O-2} = \sum_{k=0}^{2} L_{La+3,Sr+2:Cr+3,Mn+3:O-2} (y_{La+3} - y_{Sr+2})^k (y_{Cr+3} - y_{Mn+3})^k \quad (10)$$

and

$$L_{La+3,Sr+2:Cr+3,Mn+4:O-2} = \sum_{k=0}^{2} L_{La+3,Sr+2:Cr+3,Mn+4:O-2} (y_{La+3} - y_{Sr+2})^k (y_{Cr+3} - y_{Mn+4})^k \quad (11)$$

The coefficients k (0^{th}, 1st, 2nd order) act on composition-dependent Gibbs energies differently and are chosen to give the best fit to the available experimental data of compositions with both Cr and Mn on the B-site.

2.3. Thermodynamics of the oxygen release reaction

According to Panlener et al. [31], the partial molar enthalpy (Δh_{red}) and partial molar entropy (Δs_{red}) of the oxygen release reaction are related to the oxygen nonstoichiometry, δ, and oxygen partial pressure, pO_2 by the following relations in Eq. (12) and Eq. (13).

$$\left(\frac{1}{2}\right) RTpO_2 = \Delta h_{red} - T\Delta s_{red} \quad (12)$$

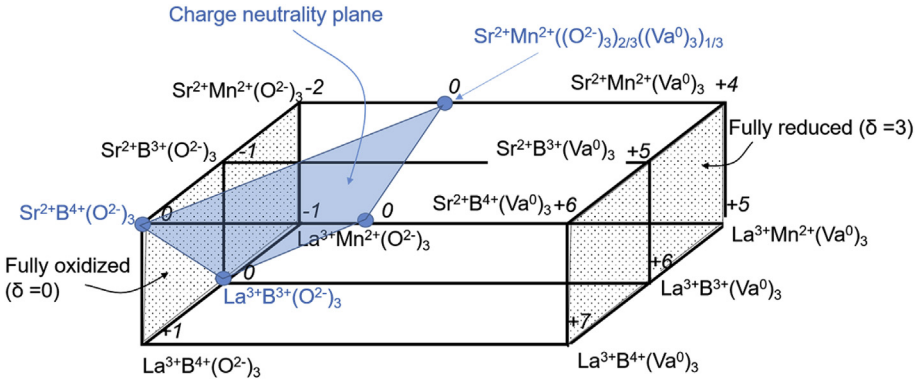

Fig. 1. Compositional representation of the perovskite system with the sublattice formula $[La^{3+}, Sr^{2+}]^{A}[Mn^{2+},Mn^{3+},Mn^{4+},Cr^{3+},Cr^{4+}]^{B}[O^{2-},Va^{0}]_3$. The charge neutrality plane (blue shaded area) represents all perovskite compositions that are allowed by electroneutrality conditions. Examples of three charge neutral compositions are highlighted in blue: $Sr^{2+}B^{4+}(O^{2-})_3$, $La^{3+}B^{3+}(O^{2-})_3$, $Sr^{2+}Mn^{2+}((O^{2-})_3)_{2/3}((Va^{0})_3)_{1/3}$, where B = Cr or Mn. Fully oxidized to fully reduced ($\delta = 3$, purely theoretic oxygen-free) perovskite compounds are highlighted by gray dot shaded area. Examples of charged end-member compositions are shown in black, e.g. $La^{3+}B^{4+}(O^{2-})_3$ and $Sr^{2+}Mn^{2+}(Va^{0})_3$ with a charge of +1 and + 4 respectively. This representation allows a visualization of potentially realizable compounds obeying charge neutrality. (For interpretation of the references to color in this figure legend, the reader is referred to the Web version of this article.)

$$\left(\frac{1}{2}\right) pO_2 = \Delta h_{\mathrm{red}}/RT - \Delta s_{\mathrm{red}}/R|_{\delta=\mathrm{constant}} \quad (13)$$

Thus, for constant δ the thermodynamic entities may be derived from the slope and intercept in a plot of oxygen partial pressure and the reciprocal temperature $1/T$ [20,23,32].

3. Results and discussion

3.1. Comparison of predicted and experimental oxygen nonstoichiometry of $La_{0.75}Sr_{0.25}Mn_{0.5}Cr_{0.5}O_{3-\delta}$

The results of the Calphad defect model are compared to experimental data on oxygen nonstoichiometry, δ, as function of oxygen partial pressure for the composition in $La_{0.75}Sr_{0.25}Mn_{0.5}Cr_{0.5}O_{3-\delta}$ in the temperature range 973 K–1273 K see Fig. 2. A strong agreement is observed for this perovskite with an equal amount of Cr and Mn on the B-site. Since the model is likewise able to reproduce and predict variations of A-site composition in the end-member compositions, i.e. $La_{1-x}Sr_xCrO_3$ and $La_{1-x}Sr_xMnO_3$ consistently, we conclude that the chosen model parameters provide the best representation of defect chemistry of the $La_{1-x}Sr_xMn_{1-y}Cr_yO_{3-\delta}$ perovskite oxide. All tests of alternative parameterizations required considerably higher (and presumably unlikely) excess energies for a comparable agreement between calculated and experimental nonstoichiometries, or the same agreement could not be reached at all. The chosen Redlich-Kister parameters accounting for non-ideal interactions between Cr- and Mn-valencies on the B-sites are listed in Table 1. For the purpose of reproducing our computations with the Thermocalc software package, we provide the complete set of thermodynamic parameters in Supporting Information in a database format [33].

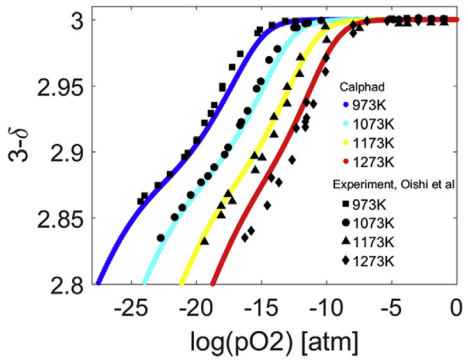

Fig. 2. Oxygen nonstoichiometry, δ, of $La_{0.75}Sr_{0.25}Cr_{0.5}Mn_{0.5}O_{3-\delta}$ as function of oxygen partial pressure in the temperature range 973 K–1273 K. Symbol markers represent data extracted from Oishi et al. [27] and colored solid lines correspond to modelled defect chemistry from Calphad.

3.2. Computed oxygen nonstoichiometry of the $La_{0.6}Sr_{0.4}Mn_{1-y}Cr_yO_{3-\delta}$ perovskite oxide

Computed oxygen nonstoichiometry data are depicted in a temperature window of 1073–1873K relevant for classic solar-to-fuel reactors in Fig. 3. We show the nonstoichiometry as function of oxygen partial pressure for four different chromium doping concentrations $y = 0$, 0.2, 0.5 and 0.9 for $La_{0.6}Sr_{0.4}Mn_{1-y}Cr_yO_{3-\delta}$, in Fig. 3a–d respectively. For all compositions, an increased oxygen release for higher temperatures and lower oxygen partial pressure is obtained. The evaluation reveals that the values are strongly dependent on the B-site doping with chromium and that the oxygen release profiles shift towards lower pO_2 for higher chromium content. Comparing for example at the highest temperature 1873 K, the composition $La_{0.6}Sr_{0.4}MnO_{3-\delta}$ reaches an oxygen nonstoichiometry of $\delta = 0.2$ at an oxygen partial pressure of $pO_2 = 10^{-5.6}$ atm In order to reach the same oxygen nonstoichiometry for a doping content of $y = 0.2$, 0.5 and 0.9 at 1873 K, the oxygen partial pressure is equal to $10^{-6.7}$ atm, $10^{-8.4}$ atm, $10^{-13.4}$ atm, correspondingly. For comparison of oxygen nonstoichiometry as function of temperature at fixed oxygen partial pressure, see Supporting Information S1.

3.3. Heat capacity of the perovskite type oxide $La_{0.6}Sr_{0.4}Mn_{1-y}Cr_yO_{3-\delta}$ by thermodynamic computation

Materials with a low heat capacity are in general desirable for the solar-to-fuel technology because the energy penalty for heating the material is lower and the efficiency thus higher. In Fig. 4, we plot modelled heat capacity, from Eq. (8), as function of temperature for solid solutions of $La_{0.6}Sr_{0.4}Mn_{1-y}Cr_yO_{3-\delta}$ with respect to chromium concentration in the entire solid solution range from $y = 0.0$–1.0. The heat capacity is plotted at a typical oxygen partial pressure for solar-to-fuel reactors of 10^{-6} atm in the temperature

Table 1
Redlich-Kister parameters for interaction between Cr and Mn on the B-site in the perovskite $La_{0.6}Sr_{0.4}Mn_{1-y}Cr_yO_{3-\delta}$.

Optimized Redlich – Kister interaction parameters, J/mol atoms $(La^{3+}Sr^{2+}, Va)(Cr^{3+}, Cr^{4+}, Mn^{2+}Mn^{3+}, Mn^{4+}, Va)(O^{2-}, Va)_3$
${}^0L_{La^{3+},\,Sr^{2+}:\,Cr^{3+},\,Mn^{3+}:O^{2-}}, = -149469$
${}^1L_{La^{3+},\,Sr^{2+}:\,Cr^{3+},\,Mn^{3+}:O^{2-}} = -130631$
${}^2L_{La^{3+},\,Sr^{2+}:\,Cr^{3+},\,Mn^{3+}:O^{2-}} = -109105$
${}^0L_{La^{3+},\,Sr^{2+}:\,Cr^{3+},\,Mn^{4+}:O^{2-}} = -112865$
${}^1L_{La^{3+},\,Sr^{2+}:\,Cr^{3+},\,Mn^{4+}:O^{2-}} = -80494$

range from 1173 K to 1873 K. It is noted, that the heat capacity increases as function of temperature for all compositions and most interestingly, it decreases for higher chromium content. We find that increasing the chromium content from $y = 0$ to a value of $y = 1.0$, decreases the heat capacity by 10% from 147 J mol^{-1} K^{-1} to a value of 132 J mol^{-1} K^{-1} at 1173 K. For perspective, the benchmark material ceria has a heat capacity that has a lower value of 80 J mol^{-1}K^{-1} [34].

3.4. Calculated thermodynamics of the oxygen release reaction as function of oxygen nonstoichiometry for $La_{0.6}Sr_{0.4}Mn_{1-y}Cr_yO_{3-\delta}$

The partial molar enthalpy and entropy of the oxygen release reaction derived from the oxygen nonstoichiometry are presented in Fig. 5. For increasing oxygen release most compositions of $La_{0.6}Sr_{0.4}Mn_{1-y}Cr_yO_{3-\delta}$ display an increase in enthalpy, whereas there is a decrease in entropy as function of oxygen release, Fig. 5a–b. In Fig. 5c, we show the Gibbs free energy change of reduction of the perovskites $La_{0.6}Sr_{0.4}Mn_{1-y}Cr_yO_{3-\delta}$ from the enthalpy and entropy as function of temperature. Importantly, this figure shows that Cr-doping results in a higher value of Δg_{red}, *i.e.* more energy is required to reduce this perovskite solid solution. Equivalently, more energy is gained by oxidation. One can predict whether the metal oxide has favorable thermodynamics for solar-to-fuel conversion by analysing the Gibbs free energy change of the entire reaction given by

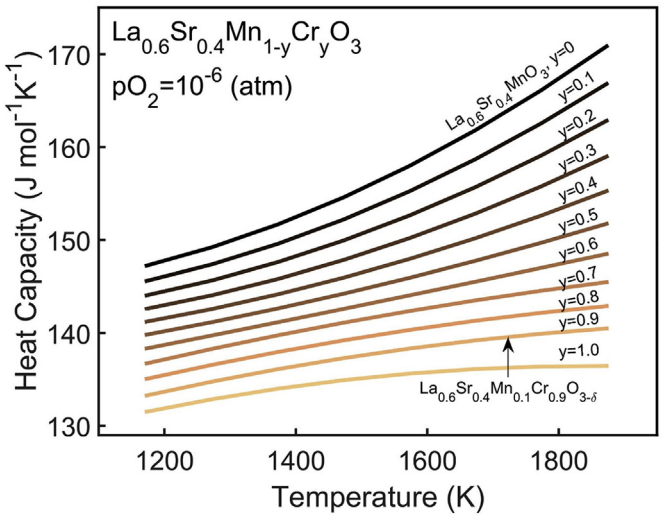

Fig. 4. Heat capacity, C_p, as function of temperature of the perovskite oxide $La_{0.6}Sr_{0.4}Mn_{1-y}Cr_yO_3$ for ($y = 0.0$, 0.1, 0.2, 0.3, 0.4, 0.5, 0.6, 0.7, 0.8, 0.9, 1.0) compiled from Calphad at an oxygen partial pressure of 10^{-6} atm.

$$\Delta g_{rxn} = -\Delta g_{red} + \Delta g_{H_2O} \quad (14)$$

where Δg_{H2O} is the Gibbs free energy change associated with water

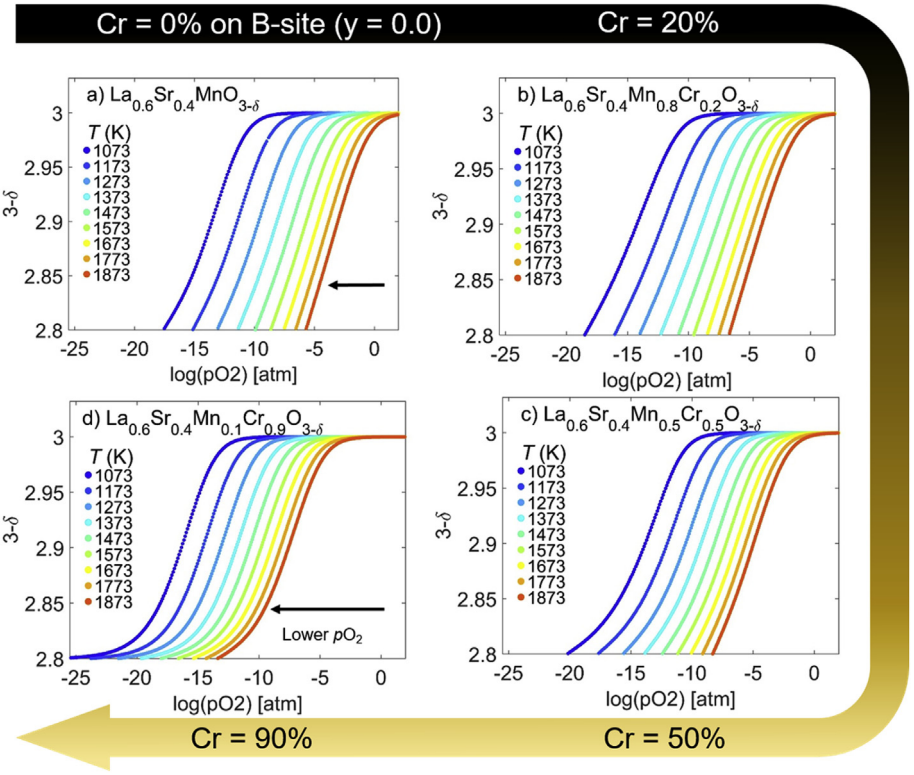

Fig. 3. Oxygen nonstoichiometry is shown versus oxygen partial pressure in a temperature window of 1073–1873 K: All data are extracted from Calphad libraries with descriptions of defect chemistry of the perovskite solid solutions $La_{0.6}Sr_{0.4}Mn_{1-y}Cr_yO_{3-\delta}$ ($y = 0.0$, 0.2, 0.5, 0.9).

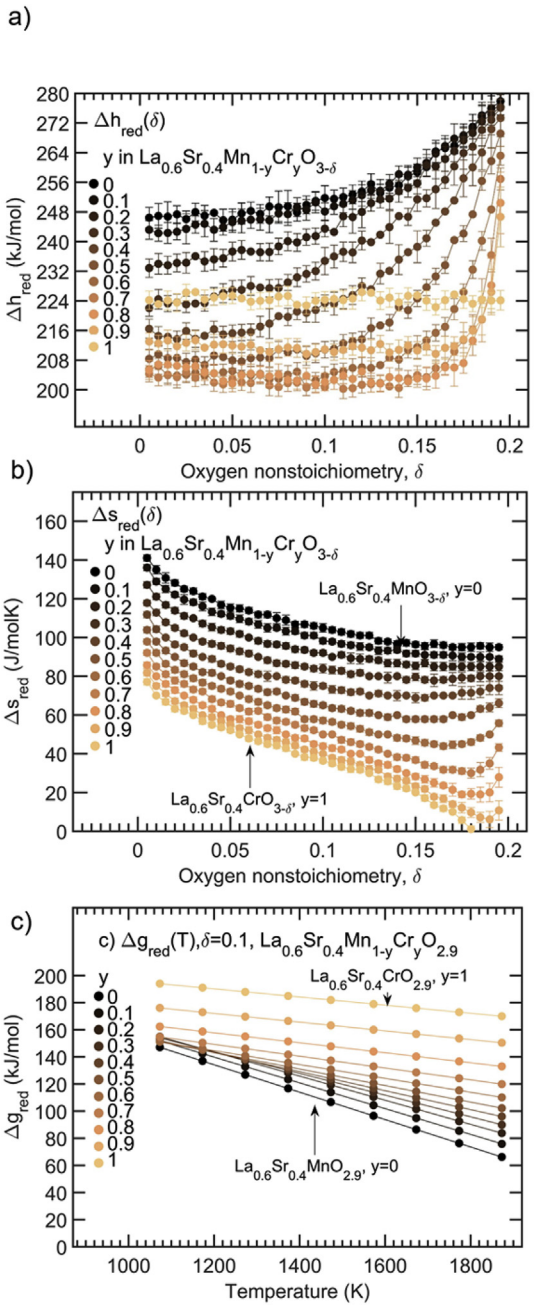

Fig. 5. Thermodynamics of the defect reaction $O_O^x + 2Me_{Me} \rightleftharpoons 1/2O_2(g) + V_O^{\cdot\cdot} + Me_{Me}^x$ as function of oxygen nonstoichiometry for the solid solutions $La_{0.6}Sr_{0.4}Mn_{1-y}Cr_yO_{3-\delta}$ (y = 0, 0.1, 0.2, 0.3, 0.4, 0.5, 0.6, 0.7, 0.8, 0.9, 1.0): (a) partial molar enthalpy, and (b) partial molar entropy derived from Calphad descriptions of oxygen nonstoichiometry versus oxygen partial pressure and temperature. (c) Gibbs free energy change calculated based on the enthalpy and entropy as function of temperature at an oxygen nonstoichiometry of $\delta = 0.1$.

splitting. When the term Δg_{rxn} is negative, the perovskite is oxidized spontaneously in the presence of water. A similar expression can be written for CO_2 splitting, but the thermodynamics of this reaction is similar and equivalent conclusions can be made on the material performance, so it will not be considered here [18,20]. As a result, it is observed that Cr-doping leads to more favorable thermodynamics for water splitting because the total Gibbs free energy of the reaction Δg_{rxn} approaches negative values.

Most importantly, it is recognized from Fig. 5c that $La_{0.6}Sr_{0.4}MnO_{3-\delta}$ has a steeper slope than $La_{0.6}Sr_{0.4}CrO_{3-\delta}$ of the Δg_{red}-function due to a large difference in the entropy. The difference in entropy has great consequences on the operation of the material, since a high value of Δg_{red} is desired for the gas splitting reaction. Considering $La_{0.6}Sr_{0.4}MnO_{3-\delta}$ for the sake of example, the Gibbs free energy of reduction, Δg_{red}, is 66 kJ mol^{-1} at a temperature 1873 K. For this material, it is necessary to lower the oxidation temperature to 1073 K to reach a value of 147 kJ mol^{-1} *viz.* it is operated best as conventional two-step metal oxide with reduction at high temperature and oxidation at a lower temperature in agreement with literature [6]. This behavior is in contrast to the material $La_{0.6}Sr_{0.4}Mn_{0.1}Cr_{0.9}O_{3-\delta}$ that shows a minor dependence on temperature and a high value of 170 kJ mol^{-1} at 1873 K. In other words, the Cr-doped material has a high thermodynamic driving force for water splitting even at high temperatures for isothermal conditions.

In Fig. 6, we summarize the relationship between the thermodynamic functions and the B-site composition. Considering an exemplary oxygen nonstoichiometry of $\delta = 0.1$, Fig. 6a, the enthalpy decreases by 20% from 251 kJ mol^{-1} to 200 kJ mol^{-1} for the composition range $y = 0$–0.7, while it increases by 16% from $y = 0.7$ to $y = 1.0$. Remarkably, the entropy decreases by 58%, Fig. 6b, when the chromium content is changed from $y = 0.0$ to $y = 0.9$. For this reason, the increase in the Gibbs free energy for the Cr-doped materials is not related to differences in the enthalpy but a very large decrease in the entropy as illustrated qualitatively by the red and green arrows in Fig. 6c.

3.5. Equilibrium hydrogen fuel yields of combined Cr- and Sr-doped lanthanum manganite produced by water splitting

Here, the effect of chromium doping on the B-site of $La_{0.6}Sr_{0.4}Mn_{1-y}Cr_yO_{3-\delta}$ on thermochemical water splitting is computed. In Fig. 7, we focus on the hydrogen fuel yield of the $La_{0.6}Sr_{0.4}Mn_{1-y}Cr_yO_{3-\delta}$ perovskite-family as function of the water concentration. The hydrogen yields are plotted for an experiment with reduction at 1773 K and $pO_2 = 10^{-6}$ atm followed by oxidation at 1273 K. Applying these reducing conditions is motivated by previous thermochemical studies of the perovskite material $La_{0.6}Sr_{0.4}MnO_{3-\delta}$ at temperatures up to 1773 K [6,15,18] indicating that the materials remain chemically stable after cycling. Substitution of manganese by chromium will further increase the chemical stability of the perovskite phase [26,35].

From the plot in Fig. 7, it is observed that the hydrogen yield of $La_{0.6}Sr_{0.4}MnO_{3-\delta}$ increases for higher water concentration and it reaches a plateau of 0.18 mol at a water concentration of $n_{H2O} = 10^4$ n_{ABO3} marked by the red dot. This means that this material will be re-oxidized completely, in a closed system by 10,000 mol of water per 1 mol of perovskite. Adding chromium to the B-site in $La_{0.6}Sr_{0.4}Mn_{1-y}Cr_yO_{3-\delta}$ results in considerably lower maximum fuel production yield, *e.g.*, $n_{H2} = 0.03$ mol for $y = 0.9$. The low fuel production given for $y = 0.9$ is due to the low reduction extents, δ_{red}, at the given conditions of temperature and oxygen partial pressure. On the other hand, less water is required to fully oxidize the material in line with the increased thermodynamic driving force observed in Fig. 3. For example, the material with the highest chromium content would be fully oxidized at a water concentration of $n_{H2O} = 10^{2.3}$ $n_{ABO3} \approx 200$ n_{ABO3}

In this context, it is crucial to recognize all energetic inputs required to produce that fuel, for instance the energy penalty for heating water is directly proportional to the amount of water that is used in the reaction.

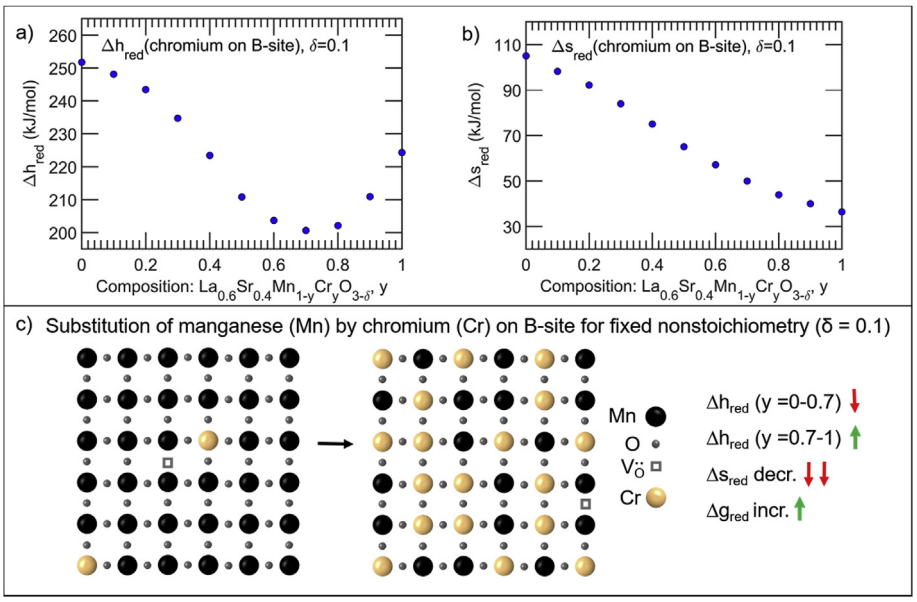

Fig. 6. a) Enthalpy and b) entropy change of the oxygen release reaction as function of chromium doping in $La_{0.6}Sr_{0.4}Mn_{1-y}Cr_yO_{3-\delta}$ at a fixed oxygen nonstoichiometry of $\delta = 0.1$. c) Illustration of substitution of manganese by chromium and the effect on the thermodynamic trends. When chromium substitutes manganese completely, the Gibbs free energy increases because the decrease in entropy is greater (illustrated qualitatively by two down arrows) than the changes in enthalpy (one up arrow).

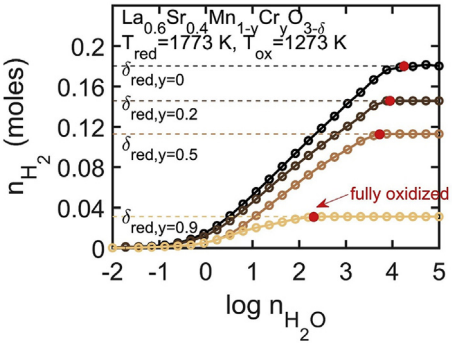

Fig. 7. Equilibrium hydrogen fuel yield (n_{H2}) per mol perovskite plotted as a function of the logarithm of the water concentration n_{H2O}. Oxidation is carried out at the temperature $T_{ox} = 1273$ K after reduction at the temperature $T_{red} = 1773$ K and $pO_2 = 10^{-6}$ atm., which results in the nonstoichiometries, δ_{red} indicated in the plot for the various compositions $La_{0.6}Sr_{0.4}Mn_{1-y}Cr_yO_{3-\delta}$ ($y = 0.0, 0.2, 0.5, 0.9$). The water concentration is in multiples of mol perovskite n_{ABO3}.

3.6. Optimized Cr-doping for improved efficiency of the thermochemical cycle

The performance of a material for the solar-to-fuel conversion process may be quantified by the thermal efficiency $\eta_{\text{solar-to-fuel}}$ [36,37]

$$\eta_{\text{solar-to-fuel}} = \frac{\text{HHV}_{H_2} n_{H_2}}{Q_{\text{total}}} \tag{15}$$

n_{H2} is the hydrogen yield per mole perovskite per cycle, HHV_{H2} is the higher heating value of hydrogen and Q_{total} is the total energy input required to produce that fuel. Here, we will set the energy penalties concerning reactor type to zero and focus on the relative performance of the materials for different conditions, so the input energy $Q_{\text{solar,mat}}$ concerns the material specific properties required to drive the reaction [6,20].

$$Q_{\text{solar,mat}} = \frac{1}{\eta_{\text{abs}}}\left(\Delta h_{H_2O|_{298K\rightarrow T_{ox}}} n_{H_2O} + \int_{T_{ox}}^{T_{red}} c_p dT + \Delta h_{\text{red}} \delta n_{ox}\right) \tag{16}$$

Here, $\Delta h_{H2O|298K\rightarrow Tox}$ is the energy required to heat the water from room temperature to the oxidation temperature, multiplied by n_{H2O} the moles of water per mole of perovskite. $\int_{T_{ox}}^{T_{red}} c_p dT$ is the sensible heat of the metal oxide for the given temperature swing and Δh_{red} is the enthalpy change for the perovskite oxide for the number of moles of perovskite being reduced. The absorption efficiency is given by $\eta_{abs} = 1 - \sigma T_{red}^4 I^{-1} C^{-1}$, where σ is the Stefan-Boltzmann constant, $I = 1$ kW m^{-2} is direct normal irradiation and C is the solar flux concentration ratio. The solar concentration ratio is set to $C = 5000$ to be consistent with earlier theoretical models [6,20] and which may be achieved with a parabolic dish design as described by Dähler et al. [38].

The yield and efficiency of thermochemical water splitting by the perovskite $La_{0.6}Sr_{0.4}Mn_{1-y}Cr_yO_{3-\delta}$ for reduction at 1773 K and $pO_2 = 10^{-6}$ atm, are plotted as function of composition and oxidation temperature in Fig. 8. Equilibrium yields and efficiency is shown in Fig. 8a–b. For further description and explanation of the efficiency, we plot the input energy $Q_{\text{solar,mat}}$ in Fig. 8c and the two most dominant input energy terms, *i.e.* sensible heat for the metal oxide and energy to heat the water to the reaction temperature in Fig. 8d. In agreement with the thermodynamic trends, chromium doping plays an influential role on the fuel production, Fig. 8a. For the material $La_{0.6}Sr_{0.4}MnO_{3-\delta}$, we observe that a lower oxidation temperature increases the energy output, reaching a maximum of 0.02 mol at 1073 K. Increasing the chromium contents, $y > 0.3$, the trend is entirely different *i.e.* lower oxidation temperature decreases the hydrogen yields. Interestingly, the material with $La_{0.6}Sr_{0.4}Mn_{0.2}Cr_{0.8}O_{3-\delta}$ increases its fuel production from 0.002 up to 0.011 when the oxidation temperature is increased from 1073 to 1773 K.

In Fig. 8b, it is observed that the solid solution

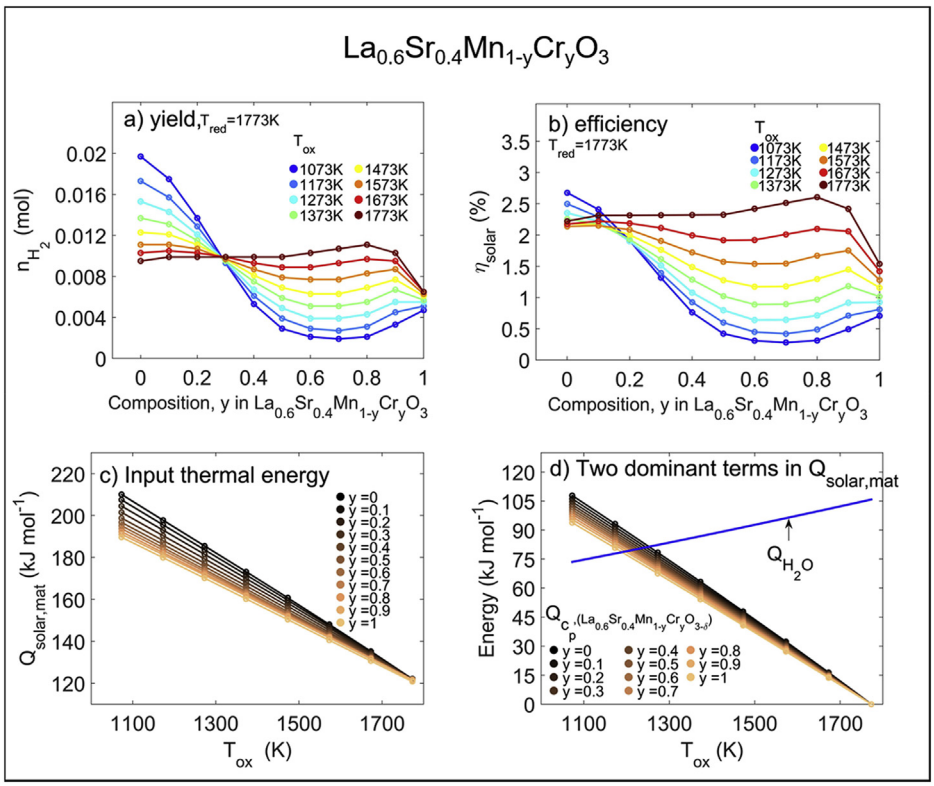

Fig. 8. Comparison of yield, efficiency and the input thermal energy for a thermochemical water splitting cycle. Calculated for the entire chromium doping range on the B-site in $La_{0.6}Sr_{0.4}Mn_{1-y}Cr_yO_3$ for y = 0.0, 0.1, 0.2, 0.3, 0.4, 0.5, 0.6, 0.7, 0.8, 0.9, 1.0. (a) Equilibrium hydrogen yields, n_{H2} as function of composition and temperature. (b) Efficiency as function of composition and temperature for a water concentration of $n_{H2O} = n_{ABO3}$. (c) Material specific solar input, $Q_{solar,mat}$ to produce the given hydrogen fuel yields. (d) The two most dominant terms in minimum required solar input to $Q_{solar,mat}$ which is the energy to heat water, Q_{H2O}, from room temperature (298 K) to the oxidation temperature T_{ox} and $Q_{cp,}(La_{0.6}Sr_{0.4}Mn_{1-y}Cr_yO_3)$ the sensible heat given by the heat capacity of the metal oxide.

$La_{0.6}Sr_{0.4}Mn_{0.2}Cr_{0.8}O_{3-\delta}$ has the highest efficiency of 2.7% for oxidation at 1773 K, which makes this material an interesting candidate for isothermal water and carbon dioxide splitting in comparison to $La_{0.6}Sr_{0.4}MnO_{3-\delta}$ which was recently considered as a promising candidate for isothermal water splitting [15]. In particular, we have recently proved that this class of perovskite exhibit improved kinetic properties at near-isothermal and isothermal temperature regimes, where this material has a higher thermodynamic driving force for water and carbon dioxide splitting [39]. In addition to a higher fuel production and efficiency of $La_{0.6}Sr_{0.4}Mn_{0.2}Cr_{0.8}O_{3-\delta}$ this material has displayed improved stability according to earlier studies in related energy technologies [26,35].

The required input energy $Q_{solar,mat}$, Fig. 8c, decreases for higher oxidation temperature because the sensible heat is lower for a smaller temperature swing as shown in Fig. 8d. This explains the relative high efficiency for $y = 0.8$ even though the fuel production is lower. Fig. 8c–d also emphasize the importance of the heat capacity since it is one of the two most dominant terms in the material specific energy input $Q_{solar,mat}$. For temperature swing cycling between 1773 K and 1073 K, the sensible heat is approximately 50% of the total required input. This is important to consider when compared to ceria that has a heat capacity that is ca. 40% lower than the perovskites reported here. For further discussion of the additional factors that ultimately lowers the efficiency due to an increase in the value of Q_{total} we refer the reader to the work of Jarrett et al. [37].

As a general remark, the fact that our computed efficiencies are below 3% for $La_{0.6}Sr_{0.4}MnO_{3-\delta}$ which is identical to the results presented in our previous benchmarked publication for these conditions, is related to the water concentration set to 1 mol of water per 1 mol of perovskites [20]. It is possible to achieve higher thermal efficiencies using a higher water concentration but this assumes highly efficient heat recuperation [6,20]. Even though we identify $La_{0.6}Sr_{0.4}Mn_{0.2}Cr_{0.8}O_{3-\delta}$ as a promising candidate compared to $La_{0.6}Sr_{0.4}MnO_{3-\delta}$ at isothermal conditions, it is important to note that the efficiency value at those conditions is the same of $La_{0.6}Sr_{0.4}MnO_{3-\delta}$, *i.e.* 2.7%, for temperature swing cycling between 1773 K and 1073 K. For perspective, Muhich et al. [16], compared four perovskites including $La_{0.6}Sr_{0.4}MnO_{3-\delta}$ to ceria and Zr-doped ceria, showing Zr-doped ceria outperformed the tested metal oxides under most of the considered conditions in terms of solar-to-fuel efficiency. In fact, the focus of this work was to demonstrate the potential of Calphad thermodynamic data libraries to accurately predict the solar-to-fuel efficiency of multicomponent oxides with 5 elements, exemplified in this case for La–Sr–Cr–Mn–O system, previously unexplored for thermochemical solar-driven syngas production. Although we acknowledge that ceria remains as the reference material in the field for its high efficiency [8,40–42], we show that applying Calphad modeling could ease the assessment and discovery of new complex materials with balanced thermodynamics and defect chemistry for higher efficiency.

4. Conclusion

We have refined and optimized a Calphad defect model of the $La_{0.6}Sr_{0.4}Mn_{1-y}Cr_yO_{3-\delta}$ perovskites by including data on $La_{0.75}Sr_{0.25}Mn_{0.5}Cr_{0.5}O_{3-\delta}$ from literature between 973 K and 1273 K, to make a predictive thermodynamic assessment of a material previously unexplored for the solar-to-fuel conversion

technology. The resulting optimized defect model of the $La_{1-x}Sr_xMn_{1-y}Cr_yO_{3-\delta}$ solution series is used to make testable predictions of oxygen nonstoichiometry, heat capacity and thermodynamics of the oxygen release reaction in a wide temperature range between 1073 K and 1873 K. From this, the following implications on the role of exchange of Mn by Cr can be emphasized: Substituting Mn with Cr on the B-site has two advantages for the solar-to-fuel technology. Firstly, it reduces the heat capacity by 10% and secondly it enhances the material's thermodynamic favorability for H_2O and CO_2 splitting near isothermal conditions.

The perovskites reported to this date such as $La_{0.6}Sr_{0.4}MnO_{3-\delta}$, are operated thermodynamically favorable in a two-step thermochemical cycle, with a high reduction temperature and low temperature for oxidation. Based on thermodynamic data, we predict that Cr substitution can be utilized to achieve higher efficiency, with respect to $La_{0.6}Sr_{0.4}MnO_{3-\delta}$ with operation near isothermal conditions. Isothermal or near isothermal solar-to-fuel production comes with operational benefits, such as reduced thermal stress on active and containment materials and it mitigates the energy required to reheat the active material as it cycles between the oxidation and reduction temperature. The composition $La_{0.6}Sr_{0.4}Mn_{0.2}Cr_{0.8}O_{3-\delta}$ reaches a maximum efficiency of 2.7% for isothermal water splitting at 1773 K. It is possible to achieve the same efficiency of 2.7% for $La_{0.6}Sr_{0.4}MnO_{3-\delta}$, but it requires temperature swing cycling between 1773 K and 1073 K. The higher efficiency at elevated temperature for the Cr substituted perovskite is related to a strong increase in $\Delta g_{red.}$. This increase is a direct consequence of a minor decrease of −16% in the enthalpy, Δh_{red}, but a much larger decrease of −58% in entropy Δs_{red}, for a change in chromium content from 0.0 to 0.9.

In conclusion, applying Calphad modeling data enables one to predict the performance of a perovskite with two A-site and two B-site cations. Although Cr substitution favors the oxidation reaction at higher temperature, the reduction extent is low which results in a low efficiency if compared with state-of-the-art ceria. However, and most importantly, the methodology presented here shows the potential of utilizing and refining thermodynamic libraries for the design of novel multicomponent redox materials with capacity to split H_2O and CO_2 to form renewable syngas, illustrating again the beneficial synergies between the Solid State Ionics and Thermochemistry communities and the discovery of novel oxides for the solar-driven fuel production.

Acknowledgements

The authors acknowledge financial support by the ETH Foundation for this work, grant number ETH-05 13-1.

Appendix A. Supplementary data

Supplementary data to this article can be found online at https://doi.org/10.1016/j.actamat.2019.07.022.

Nomenclature

$C =$ solar flux concentration ratio, dimensionless
C_p^{prv} = heat capacity of perovskite, kJ mol^{-1}
$\delta =$ oxygen nonstoichiometry
$\eta_{solar-to-fuel}$ = solar-to-fuel efficiency
η_{abs} = solar energy adsorption efficiency
$\Delta s_{red} =$ entropy of reduction of perovskite, J mol^{-1}K^{-1}
$\Delta h_{red} =$ enthalpy of reduction of perovskite, kJ mol^{-1}
$\Delta h_{H_2O|_{298K\rightarrow T_{ox}}}$ = enthalpy to heat the water from room 298 K to T_{ox}, kJ mol^{-1}
HHV_{H_2} = higher heating value of hydrogen, kJ mol^{-1}
$G =$ Gibbs free energy kJ mol^{-1}
Δg_{rxn} = Gibbs free energy change of reaction, kJ mol^{-1}
Δg_{red} = Gibbs free energy change reduction of perovskite, kJ mol^{-1}
Δg_{H_2O} = Gibbs free energy change of water dissociation, kJ mol^{-1}
$^{\circ}G_m^{prv}$ = Molar Gibbs free energy function of perovskite at standard conditions, kJ mol^{-1}
$^{\circ}G_{i:j:k}$ = Molar Gibbs free energy function of end-member compounds, kJ mol^{-1}
$^{E}G_m^{prv}$ = Excess molar Gibbs free energy of perovskite, kJ mol^{-1}
G_m^{ABO3} = Molar Gibbs free energy of perovskite, kJ mol^{-1}
$^{\circ}G_r$ = reciprocal reaction parameter
$I =$ direct normal irradiation W m^{-2}
$H =$ enthalpy, kJ mol^{-1}
$L_{i,j:\ldots:k}$ = Interaction energies, kJ mol^{-1}
L4O = $La^{3+}Mn^{4+}(O^{2-})_3$
$Mn_{Mn}^{\times}$ = Manganese ion on a manganese lattice site, neutral charge
$Mn_{Mn}^{\bullet}$ = Manganese ion on a manganese lattice site, with a single positive charge
$n_{H2O=}$ water concentration, mol
$n_{H2} =$ hydrogen yield, mol
$pO_2 =$ oxygen partial pressure, atm
Q_{total} = total energy input required to produce fuel at given conditions, kJ mol^{-1}
$Q_{solar,mat}$ = material energy input required to produce fuel at given conditions, kJ mol^{-1}
$S =$ entropy, J mol^{-1} K^{-1}
S2O = $Sr^{2+}Mn^{2+}(O^{2-})_3$
$T =$ temperature, K
T_{ox}, $T_{red} =$ oxidation and reduction temperature, K
$x =$ Sr concentration on A-site of perovskite ABO_3
$y =$ B-site Cr concentration on B-site of perovskite ABO_3
$y_i =$ the site fraction of each cation on the A-sublattice
$y_j =$ the site fraction of each cation on the B-sublattice
$y_k =$ the site fraction of O^{2-} and Va on the anion sublattice

References

[1] W.C. Chueh, C. Falter, M. Abbott, D. Scipio, P. Furler, S.M. Haile, A. Steinfeld, *High-flux solar-driven thermochemical dissociation of CO_2 and H_2O using nonstoichiometric ceria*, Science 330 (2010) 1797–1801.
[2] M. Romero, A. Steinfeld, Concentrating solar thermal power and thermochemical fuels, Energy Environ. Sci. 5 (2012) 9234–9245.
[3] A.H. McDaniel, E.C. Miller, D. Arifin, A. Ambrosini, E.N. Coker, R. O'Hayre, W.C. Chueh, J. Tong, *Sr-and Mn-doped $LaAlO_{3-\delta}$ for solar thermochemical H_2 and CO production*, Energy Environ. Sci. 6 (2013) 2424–2428.
[4] A. Bork, M. Kubicek, M. Struzik, J. Rupp, *Perovskite $La_{0.6}Sr_{0.4}Cr_{1-x}Co_xO_{3-\delta}$ solid solutions for solar-thermochemical fuel production: strategies to lower the operation temperature*, J. Mater. Chem. 3 (2015) 15546–15557.
[5] S. Dey, B. Naidu, A. Govindaraj, C. Rao, *Noteworthy performance of $La_{1-x}Ca_xMnO_3$ perovskites in generating H 2 and CO by the thermochemical splitting of H_2O and CO_2*, Phys. Chem. Chem. Phys. 17 (2015) 122–125.
[6] J.R. Scheffe, D. Weibel, A. Steinfeld, *Lanthanum–strontium–manganese Perovskites as redox Materials for solar thermochemical Splitting of H_2O and CO_2*, Energy Fuels 27 (2013) 4250–4257.
[7] H. Schulz, Short history and present trends of Fischer–Tropsch synthesis, Appl. Catal. Gen. 186 (1999) 3–12.
[8] A. de la Calle, A. Bayon, *Annual performance of a thermochemical solar syngas production plant based on non-stoichiometric CeO_2*, Int. J. Hydrogen Energy 44 (2019) 1409–1424.
[9] Q. Jiang, J. Tong, G. Zhou, Z. Jiang, Z. Li, C. Li, *Thermochemical CO_2 splitting reaction with supported $La_xA_{1-x}Fe_yB_{1-y}O_3$ (A= Sr, Ce, B= Co, Mn; $0 \leqslant x, y \leqslant 1$) perovskite oxides*, Sol. Energy 103 (2014) 425–437.
[10] A. Demont, S. Abanades, E. Beche, Investigation of perovskite structures as oxygen-exchange redox materials for hydrogen production from

thermochemical two-step water-splitting cycles, J. Phys. Chem. C 118 (2014) 12682–12692.
[11] S. Dey, B. Naidu, C. Rao, *$Ln_{0.5}A_{0.5}MnO_3$ (Ln= Lanthanide, A= Ca, Sr) perovskites exhibiting remarkable Performance in the thermochemical Generation of CO and H_2 from CO_2 and H_2O*, Chem. Eur J. 21 (2015) 7077–7081.
[12] S.M. Babiniec, E.N. Coker, J.E. Miller, A. Ambrosini, *Investigation of $La_xSr_{1-x}Co_yM_{1-y}O_{3-\delta}$ (M= Mn, Fe) perovskite materials as thermochemical energy storage media*, Sol. Energy 118 (2015) 451–459.
[13] A.M. Deml, V. Stevanovic, A.M. Holder, M. Sanders, R. O'Hayre, C.B. Musgrave, *Tunable oxygen vacancy formation Energetics in the complex perovskite oxide $Sr_xLa_{1-x}Mn_yAl_{1-y}O_3$*, Chem. Mater. 26 (2014) 6595–6602.
[14] C. Rao, S. Dey, Solar thermochemical splitting of water to generate hydrogen, Proc. Natl. Acad. Sci. 114 (2017) 13385–13393.
[15] S. Dey, C. Rao, Splitting of CO2 by manganite perovskites to generate CO by solar isothermal redox cycling, ACS Energy Lett. 1 (2016) 237–243.
[16] C.L. Muhich, S. Blaser, M.C. Hoes, A. Steinfeld, Comparing the solar-to-fuel energy conversion efficiency of ceria and perovskite based thermochemical redox cycles for splitting H_2O and CO_2, Int. J. Hydrogen Energy 43 (2018) 18814–18831.
[17] M. Takacs, M. Hoes, M. Caduff, T. Cooper, J. Scheffe, A. Steinfeld, *Oxygen nonstoichiometry, defect equilibria, and thermodynamic characterization of $LaMnO_3$ perovskites with Ca/Sr A-site and Al B-site doping*, Acta Mater. 103 (2016) 700–710.
[18] C.-K. Yang, Y. Yamazaki, A. Aydin, S.M. Haile, Thermodynamic and kinetic assessments of strontium-doped lanthanum manganite perovskites for two-step thermochemical water splitting, J. Mater. Chem. 2 (2014) 13612–13623.
[19] T. Cooper, J.R. Scheffe, M.E. Galvez, R. Jacot, G. Patzke, A. Steinfeld, Lanthanum manganite perovskites with Ca/Sr A-site and Al B-site doping as effective oxygen exchange materials for solar thermochemical fuel production, Energy Technol. 3 (2015) 1130–1142.
[20] A.H. Bork, E. Povoden-Karadeniz, J.L. Rupp, Modeling thermochemical solar-to-fuel conversion: CALPHAD for thermodynamic assessment studies of perovskites, exemplified for (La, Sr) MnO_3, Adv. Energy Mater. 7 (2017) 1601086.
[21] P.S. Devi, M.S. Rao, Preparation, structure, and properties of strontium-doped lanthanum chromites: $La_{1-x}Sr_xCrO_3$, J. Solid State Chem. 98 (1992) 237–244.
[22] M. Kubicek, A.H. Bork, J.L. Rupp, Perovskite oxides–a review on a versatile material class for solar-to-fuel conversion processes, J. Mater. Chem. A 5 (2017) 11983–12000.
[23] M.J. Ignatowich, A.H. Bork, T.C. Davenport, J.L.M. Rupp, C.-K. Yang, Y. Yamazaki, S.M. Haile, *Thermo-kinetic Limitation in fuel production Rates from $La_{1-x}Sr_xMnO_{3-\delta}$ in thermochemical cycling*, MRS Commun. 7 (2017) 873–878.
[24] I. Al-Shankiti, B.D. Ehrhart, A.W. Weimer, Isothermal redox for H2O and CO2 splitting–A review and perspective, Sol. Energy 156 (2017) 21–29.
[25] E. Povoden-Karadeniz, M. Chen, T. Ivas, A. Grundy, L. Gauckler, *Thermodynamic modeling of La_2O_3–SrO–Mn_2O_3–Cr_2O_3 for solid oxide fuel cell applications*, J. Mater. Res. 27 (2012) 1915–1926.
[26] S. Tao, J.T. Irvine, S.M. Plint, *Methane oxidation at redox stable fuel cell electrode $La_{0.75}Sr_{0.25}Cr_{0.5}Mn_{0.5}O_{3-\delta}$*, J. Phys. Chem. B 110 (2006) 21771–21776.
[27] M. Oishi, K. Yashiro, K. Sato, J. Mizusaki, T. Kawada, *Oxygen nonstoichiometry and defect structure analysis of B-site mixed perovskite-type oxide (La, Sr)(Cr, M) $O_{3-\delta}$ (M = Ti, Mn and Fe)*, J. Solid State Chem. 181 (2008) 3177–3184.
[28] W.Z. Zhu, S. Deevi, Development of interconnect materials for solid oxide fuel cells, Mater. Sci. Eng. A 348 (2003) 227–243.
[29] M. Hillert, The compound energy formalism, J. Alloy. Comp. 320 (2001) 161–176.
[30] O. Redlich, A. Kister, Algebraic representation of thermodynamic properties and the classification of solutions, Ind. Eng. Chem. 40 (1948) 345–348.
[31] R. Panlener, R. Blumenthal, J. Garnier, A thermodynamic study of non-stoichiometric cerium dioxide, J. Phys. Chem. Solids 36 (1975) 1213–1222.
[32] J.R. Scheffe, A. Steinfeld, Thermodynamic analysis of cerium-based oxides for solar thermochemical fuel production, Energy Fuels 26 (2012) 1928–1936.
[33] B. Sundman, B. Jansson, J.-O. Andersson, The thermo-calc databank system, Calphad 9 (1985) 153–190.
[34] M. Zinkevich, D. Djurovic, F. Aldinger, Thermodynamic modelling of the cerium–oxygen system, Solid State Ion. 177 (2006) 989–1001.
[35] T. Nakamura, G. Petzow, L. Gauckler, *Stability of the perovskite phase $LaBO_3$ (B= V, Cr, Mn, Fe, Co, Ni) in reducing atmosphere I. Experimental results*, Mater. Res. Bull. 14 (1979) 649–659.
[36] A. Steinfeld, Solar thermochemical production of hydrogen––a review, Sol. Energy 78 (2005) 603–615.
[37] C. Jarrett, W. Chueh, C. Yuan, Y. Kawajiri, K.H. Sandhage, A. Henry, Critical limitations on the efficiency of two-step thermochemical cycles, Sol. Energy 123 (2016) 57–73.
[38] F. Dähler, M. Wild, R. Schäppi, P. Haueter, T. Cooper, P. Good, C. Larrea, M. Schmitz, P. Furler, A. Steinfeld, Optical design and experimental characterization of a solar concentrating dish system for fuel production via thermochemical redox cycles, Sol. Energy 170 (2018) 568–575.
[39] A.J. Carrillo, A.H. Bork, T. Moser, E. Sediva, Z.D. Hood, J.L.M. Rupp, *Modifying $La_{0.6}Sr_{0.4}MnO_3$ Perovskites with Cr Incorporation for fast isothermal CO2-splitting Kinetics in solar-driven thermochemical cycles*, Adv. Energy Mater. (2019), 1803886.
[40] Y. Hao, C.-K. Yang, S.M. Haile, High-temperature isothermal chemical cycling for solar-driven fuel production, Phys. Chem. Chem. Phys. 15 (2013) 17084–17092.
[41] R. Bader, L.J. Venstrom, J.H. Davidson, W. Lipinski, Thermodynamic analysis of isothermal redox cycling of ceria for solar fuel production, Energy Fuels 27 (2013) 5533–5544.
[42] B.D. Ehrhart, C.L. Muhich, I. Al-Shankiti, A.W. Weimer, System efficiency for two-step metal oxide solar thermochemical hydrogen production–Part 2: impact of gas heat recuperation and separation temperatures, Int. J. Hydrogen Energy 41 (2016) 19894–19903.